JOURNAL OF SPACECRAFT AND ROCKETS
Vol. 39, No. 3, May–June 2002

Particle-in-Cell with Monte Carlo Simulation of SPT-100 Exhaust Plumes

Francesco Taccogna,* Savino Longo,† and Mario Capitelli‡
University of Bari, 70126 Bari, Italy

A two-dimensional axisymmetric numerical code is developed for the simulation of a Hall thruster plume operating in various ambient plasmas. The code is based on a combination of particle simulation for the ionic components (Xe^+ and Xe^{++}) and fluid computational techniques for electrons. In particular, we have used the Boltzmann relation modified in order to allow for the effect of nonisothermal electron temperature based on the adiabatic approximation. In our model several solutions, which have been sparsely considered in previous works, are jointly adopted. In particular, the electric field is computed by solving the Poisson equation without assuming quasi-neutrality, which often is violated in the near-field plume region; and collision processes are included by using two new techniques, the ion-neutral test-particle Monte Carlo collision model and the Nanbu cumulative small-angle collision theory for ion-ion coulombic collisions. Comparisons with experimental data suggest that the present simulation is accurately modeling the physics of the very near-field region of the plume.

Nomenclature

$\boldsymbol{B}$	=	magnetic induction, T
$\boldsymbol{E}$	=	electric field, Vm^{-1}
e	=	electric charge constant, 1.602×10^{-9} C
$\boldsymbol{g}$	=	relative velocity, ms^{-1}
j	=	ion current density, Am^{-2}
k_B	=	Boltzmann's constant, 1.381×10^{-23} JK^{-1}
L_ρ	=	Larmor radius, m
$\ell n \Lambda$	=	Coulombic logarithm
M	=	macroparticle mass, kg
m_i	=	Xe ion mass, 2.18×10^{-25} kg
n	=	number density, m^{-3}
P	=	pressure, Pa
p	=	probability
Q	=	macroparticle charge, C
R_s	=	random number
r	=	radial coordinate, m
S	=	shape factor
T	=	temperature, K
V	=	volume, m^3
$\boldsymbol{v}$	=	velocity, ms^{-1}
z	=	axial coordinate, m
α	=	divergence angle, deg
ε_0	=	vacuum permittivity, 8.854×10^{-12} $N^{-1}m^{-2}C^2$
λ	=	mean free path, m
λ_D	=	debye length, m
ν	=	collision frequency, s^{-1}
ρ	=	charge density, cm^{-3}
σ	=	collision cross section, m^{-2}
ϕ	=	electric potential, V
φ	=	azimuthal angle, deg
χ	=	deflection angle, deg
ω	=	plasma frequency, s^{-1}

Subscripts

A	=	anode value
C	=	cathode value
e	=	electron component
ex	=	charge exchange
f	=	fast particle
fit	=	interpolated measurement
i	=	ion component
j	=	radial node index
k	=	axial node index
n	=	neutral component
r	=	radial component
ref	=	reference value
s	=	slow particle
te	=	thruster's exit value
z	=	axial component
φ	=	tangential component
∞	=	cutoff value

Superscripts

PIC	=	particle-in-cell weighting
Ruy	=	Ruyten weighting
(t)	=	iteration index
$+$	=	single-ionized particle
$++$	=	double-ionized particle

Received 14 February 2001; revision received 22 November 2001; accepted for publication 13 December 2001.

*Ph.D. Student, Chemistry Department.
†Associate Professor, Chemistry Department. Member AIAA.
‡Full Professor, Chemistry Department. Member AIAA.

Introduction

THE modeling of electric thruster plumes is a very important issue in view of the increasing importance of such propulsion in all space applications when specific impulse, and not just power, is important, that is, for satellite guidance, orbit transfer, and deep space exploration projects. It is now recognized that only a rigorous and detailed modeling at the level of kinetic equations, and not mere macroscopic models based on fluid dynamics, can include the collisional and dynamic effects that can lead to contamination of the satellite surfaces.

Indeed, an electric thruster, such as the Stationary Plasma Thruster SPT-100, in operation produces a variety of effluents. These include high-energy ions Xe^+, Xe^{++}; neutral propellant atoms; electrons emitted to neutralize the positive space charge; low-energy charge-exchange (CEX) ions created by collisions between ions and unionized propellent in which electrons are transferred. These CEX ions are strongly influenced by the self-consistent electric fields. These fields cause CEX ions to propagate radially and to flow upstream, and in doing so they also gain energy. CEX ions, therefore, can be deflected back towards the spacecraft, possibly causing contamination and degradation by sputtering on components even when located beyond the line of sight of the exhaust beam. Furthermore, the ability to simulate the plume of these devices permits a wider variety of operating conditions to be tested and also eliminates the

influence of the experimental devices. Although many test chambers can be maintained at pressures of fractions of mPa, the operating conditions of these devices give relatively low densities, and thus interactions between the plasma and background gas are to be expected. Also, the walls of the chamber can influence the plasma. Therefore, the plume of the SPT-100 has been modeled in several studies.[1–10] In this paper a two-dimensional, hybrid axisymmetric particle-in-cell (PIC)[11–13] model using test-particle Monte Carlo (TPMC) (Refs. 14 and 15; also Mitsui, K., University of Bari, Bari, Italy, personal communication, Sept. 1999) collisions to predict the charge-exchange ion environment is presented. Ions and neutrals are treated as test particles and modeled directly, respectively, by the PIC and direct-simulation Monte Carlo (DSMC) methods (Refs. 16 and 17; also Markelov, G. N., University of Bari, Bari, Italy, personal communication, March 2000), whereas the electrons are assumed collisionless and unmagnetized, that is, to follow a Boltzmann-like distribution modified in order to allow for the effect of nonisothermal electron temperature. The electron temperature is calculated on the basis of the adiabatic approximation. This model improves over the ones already in the literature because the electric potential distribution is obtained from the Poisson equation without assuming the quasi-neutral plasma hypothesis. However experimental results[6] indicate that the potential increases with electron density in some regions, in contrast with the inversion of the Boltzmann relationship. Moreover, the magnetostatic field is assumed bipolar[2] while ion/neutral injection conditions are given by data fits[18] of the measurements of Bishaev and Kim.[19] The code has been tested against several ground measurements showing good agreement.

The layout of the paper is as follows. The physical description of the SPT-100 plume analyzing the thruster effluents is reviewed. Then the selected computational model is presented, and in particular the PIC model is described as well as the method for collision treatment. Results are presented and discussed with comparison to experimental measurements.

Physical Model

Figure 1 shows the SPT-100. The plasma column is contained within two coaxial dielectric cylinders, with the anode being at one end of the channel, the exhaust at the other end, and the cathode outside the column. The propellant is injected from the anode side (and also inside the cathode), whereas the electrons are injected from the cathode side. A system of coils inside the inner cylinder and outside the outer cylinder generates a radial magnetic field with a maximum next to the exhaust, which must be used to confine the electrons, and thus the electron impact ionization is considerably increased. The positive ions produced in the channel are almost insensitive to the magnetic field and undergo practically no collisions in the column. They are accelerated toward the exhaust and reach kinetic energies closely corresponding to the potential drop across the column. Table 1 reports numerical values for parameters in a typical operative condition for SPT-100, which have been used in the present simulation as the default.

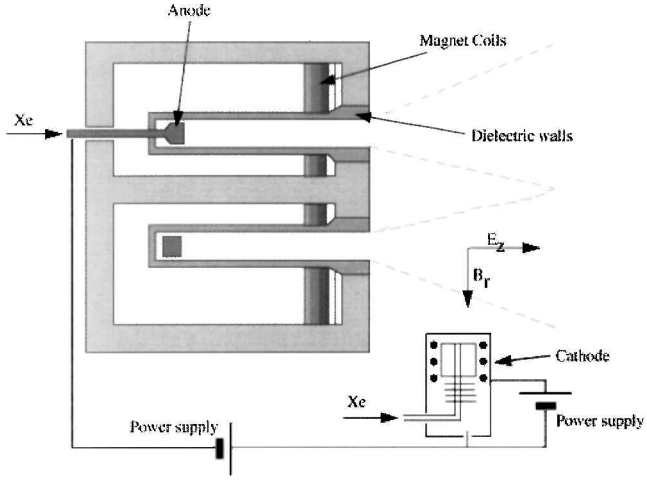

Fig. 1 SPT-100 schematic representation.

Table 1 SPT-100 performance parameters

Parameter	Value
Outer insulator radius R_2	50 mm
Inner insulator radius R_1	28 mm
Thrust T	40 mN
Voltage ϕ_D	200 V
Current i_D	3.2 A
Mass flow rate $\dot{m}$	5 mg/s
Specific impulse I_s	1600 s
Power P	1300 W
Total efficiency η_T	0.33
Ionization efficiency η_U	0.69
Acceleration efficiency η_A	0.96
Double-charged percentage η_P	0.1

Table 2 Efficiencies of the SPT-100 for 5 mg/s of xenon and for different discharge voltages[20]

ϕ_D, V	η_U	η_A	η_P	η_T
150	0.45	0.96	0.1	0.23
200	0.69	0.96	0.1	0.33
250	0.82	0.96	0.2	0.39
300	0.88	0.95	0.2	0.39
350	0.99	0.95	0.2	0.39

Table 3 Efficiencies of the SPT-100 for a discharge voltage of 300 V and for different xenon mass flow rate[20]

$\dot{m}$, mg/s	η_U	η_A	η_P	η_T
3	0.71	0.90	0.1	0.30
4	0.81	0.90	0.1	0.34
5	0.88	0.89	0.1	0.39
6	0.93	0.89	0.1	0.42
7	0.95	0.88	0.1	0.44

The plume model used in this study accounts for the following thruster effluents: 1) fast (>10-km/s) propellant beam ions; 2) unionized propellant neutrals; 3) slow (initially thermal) propellant ions created from CEX collisions; 4) neutralizing electrons. Because of the particular geometry of the problem, some elements are given in terms of axisymmetric coordinates (r, z).

Beam Ions

Charged particles are loaded into the simulation at each time step to simulate the exit flow. The ion exit conditions are[10]

$$v_i^+ = \frac{T\left(1+\eta_P\sqrt{2}\right)}{\dot{m}\eta_U\eta_A(1+2\eta_P)(\sin\bar{\alpha}/\bar{\alpha})^2}$$

$$\dot{m}_i^+ = \frac{T}{v_i^+(1+2\eta_P)(\sin\bar{\alpha}/\bar{\alpha})^2} \tag{1}$$

$$v_i^{++} = \sqrt{2}\cdot v_i^+, \qquad \dot{m}_i^{++} = \sqrt{2}\cdot\eta_P\dot{m}_i^+ \tag{2}$$

On the basis of efficiency calculated for different discharge voltages (see Table 2, where the xenon mass flow rate is 5 mg/s) and for different mass flow rate[20] (see Table 3, where the discharge voltage is 300 V), various operating conditions are simulated. The ion distribution on the exit plane is deduced after Oh and Hastings.[2] Further studies[18] argued against the mathematical expressions reported in their work claiming that the experimental data considered were not fully pertinent with the actual geometry of the thruster examined. A revision of the Oh–Hastings expressions is determined from an empirical model developed by Boccaletto[18] from experimental measurements of the ion current density.[19] These quantities represent linear fits of experimental data and give the magnitude and direction of the ion current as a function of radial position r between $R_1 = 0.028$ and $R_2 = 0.049$ m (Figs. 2a and 2b):

$$j_{\text{fit}}(r) = -1.9787241\times10^3 + 1.2974556\times10^7\cdot r^2 - 6.3929319\times10^8\cdot r^3 + 1.1640206\times10^{10}\cdot r^4 - 7.4550791\times10^{10}\cdot r^5 \tag{3}$$

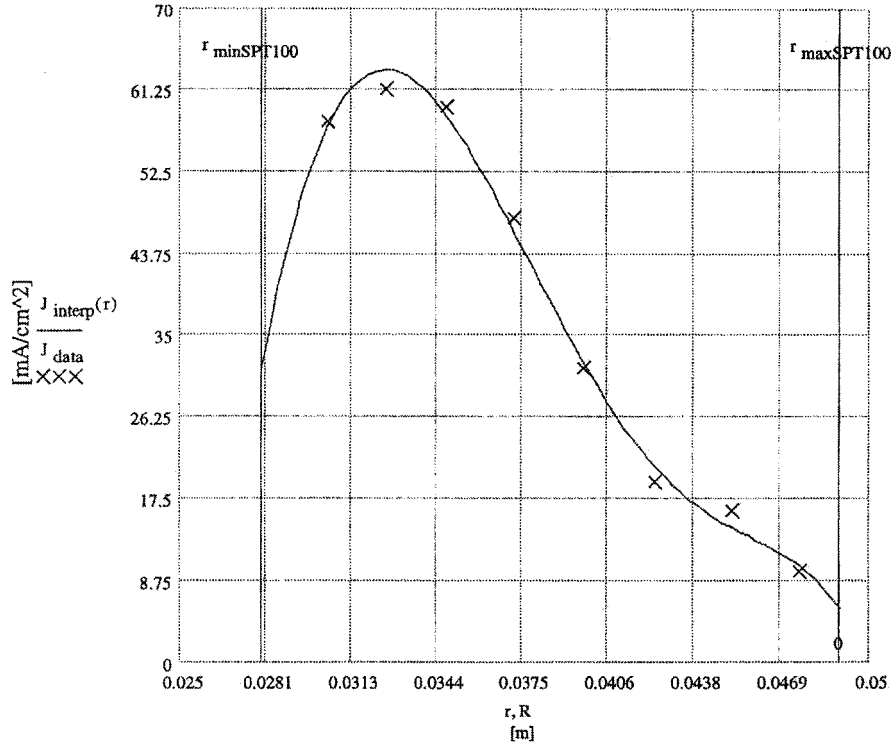

Fig. 2a Plot of ion density current at the exit plane.[18]

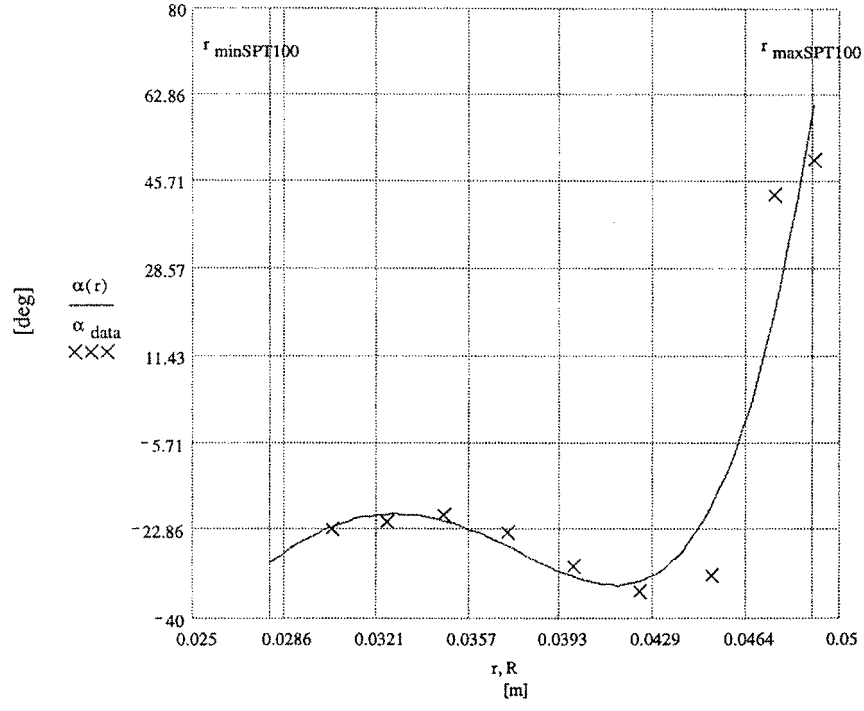

Fig. 2b Plot of divergence angle at the exit plane.[18]

$$\alpha_{\text{fit}}(r) = -1.6672237 \times 10^6 \cdot r^2 + 1.3436936 \times 10^8 \cdot r^3 - 3.6299391 \times 10^9 \cdot r^4 + 3.2502724 \times 10^{10} \cdot r^5 \quad (4)$$

A model for the ion distribution is derived by assuming that ions leave the thruster with a uniform drift velocity provided by Eq. (1). Equation (3) can thus be normalized by the integrated beam current density to give

$$p = 64.0559316 - 8.0649854 \times 10^3 \cdot r + 3.9310537 \times 10^5 \cdot r^2 - 9.3165633 \times 10^6 \cdot r^3 + 1.0847813 \times 10^8 \cdot r^4 - 4.9911403 \times 10^8 \cdot r^5 \quad (5)$$

which represents the probability that an ion crossing the exit plane has a radial position less than r.

Neutral Efflux

Although the neutral propellant atoms in a stationary plasma thruster exhaust beam account for about 10% of the total xenon mass flow, the neutral density is comparable to the beam ion density as a result of the much lower thermal velocity compared to the ion velocity. The neutrals originate both from the anode and cathode as given by the neutral mass flow rates

$$\dot{m}_n = \dot{m}_{\text{nA}} + \dot{m}_{\text{nC}} = \dot{m}(1 - \eta_U \eta_A) \quad (6)$$

The flow through the cathode is neglected because it is three-dimensional and difficult to include in an axially symmetric simulation. In any case at a typical operating condition the flow rate through the cathode is only 6% of that through the anode. To define a suitable distribution of neutrals across the exit section of the thruster, on the basis of the Ref. 21 Boccaletto has calculated the numbers of xenon atoms (per unit of surface and per unit of time and expressed in $m^{-2}s^{-1}$) flowing across the thruster exit section at radial distance (expressed in meters):

$$n_n = 8.0164474 \times 10^{20} + 5.100755 \times 10^{23} \cdot r - 4.8171475 \times 10^{25} \cdot r^2 + 1.39654 \times 10^{27} \cdot r^3 - 1.2727662 \cdot r^4 \quad (7)$$

At the thruster exit the un-ionized propellent is modeled at sonic condition based on a temperature of 1000 K with a neutral velocity of 325 m/s, which agrees well with experiments with a similar Hall thruster.[22]

Neutralizing Electrons

The time and space scale of electron dynamic is much smaller (490 times) than that of the ions. For this reason, we model the electrons using a fluid rather than a particle model. The most general momentum balance for the electrons is

$$\frac{\partial \boldsymbol{v}_e}{\partial t} + \boldsymbol{v}_e \cdot \nabla \boldsymbol{v}_e = -\frac{e}{m_e}(\boldsymbol{E} + \boldsymbol{v}_e \times \boldsymbol{B}) - \frac{\nabla P_e}{m_e n_e} - \boldsymbol{R}_e \quad (8)$$

where $\boldsymbol{v}$ here indicates the fluid (averaged) velocity to distinguish from the particle one used in the particle mover. The collisional drag terms

$$\boldsymbol{R}_e = \nu_{ei}(\boldsymbol{v}_e - \boldsymbol{v}_i) + \nu_{en}(\boldsymbol{v}_e - \boldsymbol{v}_n)$$

for the plasma density and temperatures produced by a Hall thruster can be neglected (the ratio of the collision frequency to the plasma frequency is much less than one). Still for the electron timescale the unsteady and inertia terms can be neglected. (The electrons cannot leave a region in a large group without a large charge imbalance.)

Concerning the magnetic induction $\boldsymbol{B}$, we can deduce that the perturbation produced by the current flux to the extention of applied magnetic field into the plume region is negligible, and the problem is simply electrostatic in relation to the self-consistency. Moreover, the applied magnetic field in the far plume rapidly becomes negligible: for a typical Hall effect thruster[2,20,23] magnetic field is less than 0.001% of the peak value (4×10^2 G) at a distance of about 0.2 m (Fig. 3). In the region close to the exit plane ($z < 0.2$ m), the magnetic induction effects cannot be neglected; nevertheless, in such a region collisional effects are more important. Although the electron mean free path in such region is considerably larger than typical thruster dimension (ranging between 10–100 m), collisions still occur with thruster walls. A rapid estimate of the electrons gyro radius (0.05 m) cleary shows that collisions with thruster walls occur with a frequency in the same order as the electron cyclotron frequency (estimates of plasma parameters in plume are reported in Table 4). Therefore, electrons experience a short acceleration time between collisions, and $\boldsymbol{v}_e$ remains relatively small. For this reason

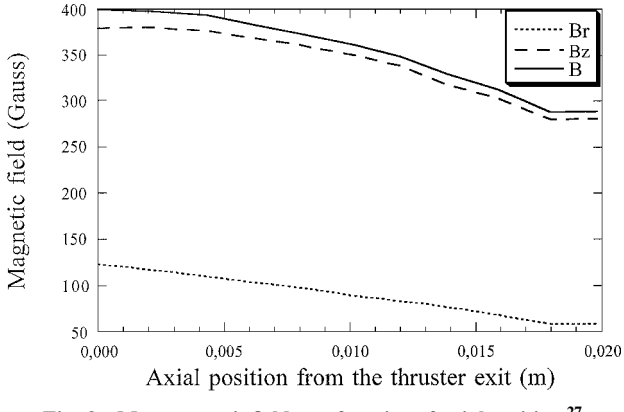

Fig. 3 Magnetostatic field as a function of axial position.[27]

Table 4 Estimates of fundamental plasma parameters in plume[5]

Plume parameter	Axial distance from thruster exit plane 0.2 m	1 m
$L_{\rho,e}$	5.4 cm	540 cm
$L_{\rho,i\text{-ex}}$	10.3 m	>1,000 m
$L_{\rho,i\text{-beam}}$	230 m	>20,000 m
λ_{en}	908 m	>20,000 m
λ_{ee}	26 m	660 m
λ_{ei}	35 m	880 m
λ_{ii}	170 m	>3,000 m

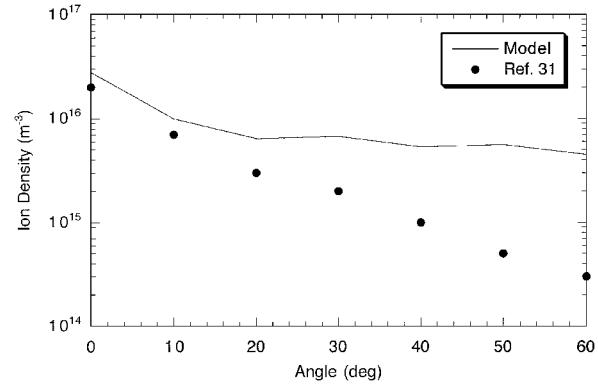

Fig. 4 Comparison of Xe^+ number density at a radial distance of 50 cm.

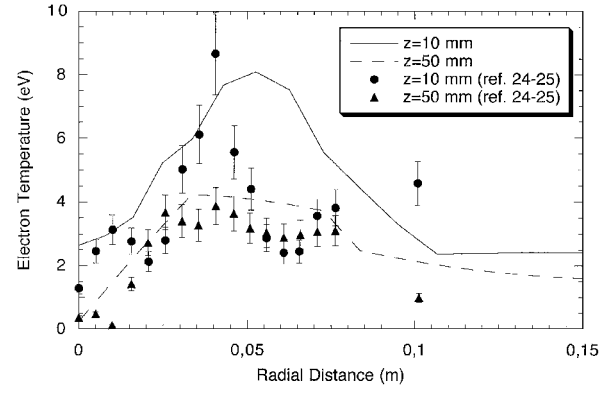

Fig. 5 Comparisons of radial profiles of electron temperature at different axial locations.

an acceptable approximation would be to neglect the magnetic induction effect in the momentum conservation equation (being small either $\boldsymbol{B}$ itself or $\boldsymbol{v}_e$).

Considering for a moment a uniform electron temperature and assuming a perfect gas behavior, the solution of momentum equation corresponds to the well-known Boltzmann barometric equation

$$n_e(r, z) = n_{\text{ref}} \exp\{e[\phi(r, z) - \phi_p]/k_B T_e\} \quad (9)$$

where the n_{ref} are calculated equating the electron density to ion density at thruster exit plane and ϕ_p is the electric potential at the thruster exit plane. Measurements of Kim[24,25] (Figs. 4 and 5) indicate a relationship between the strong varying ion density and the electron temperature. The ion density quickly (>20 cm from the thruster's exit) becomes much more homogeneous, and thus we can consider a uniform electron temperature only in far-field plume region. In the very near one the variation of the electron temperature, however, is much less than that of the plasma density because of the high electron thermal conductivity. For this reason Eq. (9) is used with a variable temperature given by the Poisson adiabatic equation (the electrons are assumed to act as an expanding fluid at isentropic conditions):

Table 5 Simulation parameters

Parameter	Value
Domain size (L_r, L_z)	1.2×1.5 m
Grid (N_r, N_z)	50×40
Ratio of radial cell-size progression β	1.03976
Ratio of axial cell-size progression β'	1.11388
Thruster size (S_1, S_2)	0.1×0.25 m
Time step Δt	1.6×10^{-7} s
Weight of macroparticles w	6.7×10^{8}
Macroions injected at each time step (N_{Xe^+}, $N_{Xe^{++}}$)	(600, 60)
Number of run to reach the steady state N_{tot}	40,000
Total number of macroparticles N_p	10^6
Potential at the thruster's exit ϕ_{te}	10 V
Reference electron density n_{ref}	1.8×10^{16} m^{-3}
Reference electron temperature T_{ref}	1 eV
Ion-neutral collision parameters (β_∞, A)	(3,1.25×10^5 J^4)

Table 6 Background plasma parameters

Ambient plasma	Pressure, Pa	Neutral temperature, K	Electron temperature, eV	Magnetic field, G
Laboratory	2.7×10^{-3}	295	4.2	0
LEO	3×10^{-9}	1160	0.1	0.3
GEO	0	0	0	0

$$T_e(j,k) = T_{ref}\left[\frac{n_e(j,k)}{n_{ref}}\right]^{(\gamma-1)} \tag{10}$$

where $\gamma = c_p/c_v$ is the ratio of specific heats (equal to $\frac{5}{3}$ for monoatomic gases) and the constant T_{ref} is chosen to closely match the electron measurements of Kim[24,25] (Table 5 and Fig. 5).

Background Gas

Three very different ambient conditions can be studied: 1) the laboratory plasma environment, 2) the low-Earth-orbit (LEO) plasma environment, and 3) the geosynchronous-Earth-orbit (GEO) plasma environment. For the first, ambient, ground-based experiments have a finite back pressure determined by the capacity of the pumping system. Although this system usually gives a density well below the exit density of the neutrals, the two values become comparable in the far plume. Thus, the background gas must be included in the simulation. This background is assumed to be composed entirely of xenon neutrals because the beam ions move at much higher speeds, and thus they leave the domain more easily. The background particles are not simulated directly because it is not necessary to update their positions or know their exact properties. Instead particles are created in each cell with velocity sampled from a Maxwellian distribution at 295 K. The background density is assumed to be uniform and calculated on the basis of the ideal gas law with a backpressure $P = 2.7$ mPa. It is not necessary to model collisions between pairs of background atoms. It is assumed that the background distribution is unchanged with collisions. This assumption is reasonable because the largest change would be a result of the fast atoms created by charge-exchange reactions. Their density is estimated at about three orders of magnitude below the total background density for the case under consideration. However we model the ion-background charge-exchange collisions because at a distance of more than a few centimeters from the exit plane the background neutrals become the dominant source of CEX ion production. The importance of the second ambient derives from the presence of the geomagnetic field (with strengths of 0.3 G typical of the LEO). For the third ambient, the GEO is assumed similar to a vacuum ambient because the actual pressures are on the order of 10–100 torr and the geomagnetic field strenghts of 0.001 G. The parameters characterizing the ambient cases are summarized in Table 6.

Numerical Model

The gas-phase transport process implies collective and collisional events, which are described by a convection term in the total derivative D and a collision term J, respectively:

$$\frac{\partial f}{\partial t} = -\boldsymbol{D}f + \boldsymbol{J}f \tag{11}$$

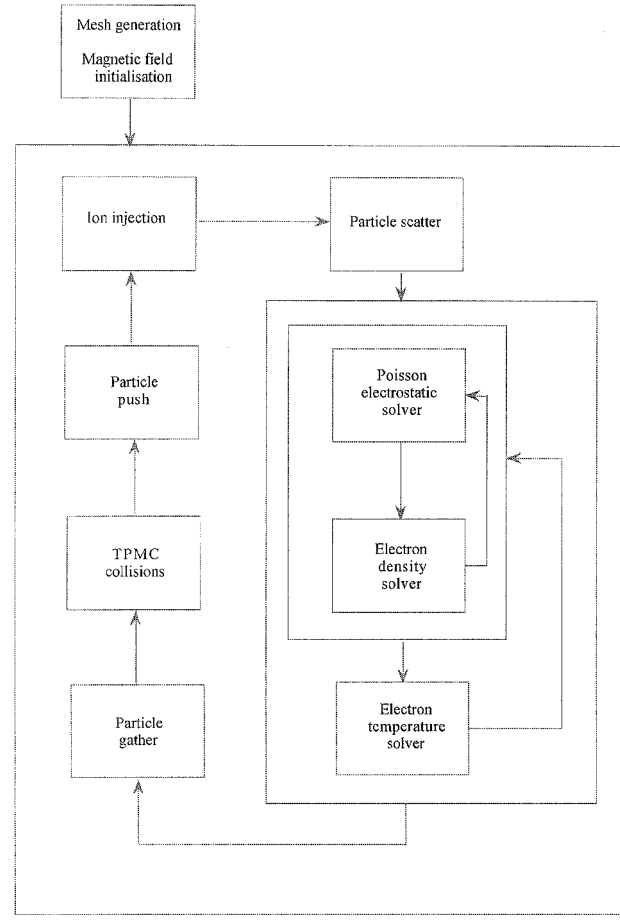

Fig. 6 Flowchart scheme of the computational model.

where

$$\boldsymbol{D}f = \boldsymbol{v}\cdot\frac{\partial f}{\partial \boldsymbol{x}} + \frac{\boldsymbol{F}}{M}\cdot\frac{\partial f}{\partial \boldsymbol{v}}, \qquad \boldsymbol{J}f = \int (f'f_1' - ff_1)g\sigma \, d\Omega \, d\boldsymbol{v}_1$$

According to the principle of uncoupling introduced by Bird,[16] the molecular motion and intermolecular collisions can be uncoupled over a small time interval Δt:

$$f(\boldsymbol{v}, \boldsymbol{x}, \Delta t) = (1 + \Delta t\boldsymbol{J})(1 - \Delta t\boldsymbol{D})\, f(\boldsymbol{v}, \boldsymbol{x}, 0) \tag{12}$$

[that is, all molecules are moved collectively under imposed and self-consistent fields over Δt (stage A) and next the collisions are computed by fixing the molecular positions (stage B)]. The treatment of stage A involves the PIC technique, where ions are considered as macroparticles and their charge is deposited onto a computational grid. (Each macroparticle represents many actual particles and w is the real to macroparticle ratio.) From this charge density Poisson's equation for electrostatic potential is solved, and the particles are moved under the influence of this self-consistent electric field and of the applied magnetostatic field. This procedure is repeated for many time steps following the flowchart shown in Fig. 6.

Grid Structure and Boundary Conditions

The computational domain extends 1.5 m in the axial direction and 1.2 m in the radial direction. To include some of the backflow region, the thruster exit plane is located at an axial distance of 25 cm from the start of the domain. The grid is nonuniform to handle more efficiently the highly nonuniform density distribution in the plume. Because the grid cell size should be on the order of the Debye length, which scales with plasma density as $n^{-1/2}$, the grid is linearly stretched in the r and z direction from the thruster exit to follow the increase in the Debye length caused by the density decrease, which is assumed to decay as $1/(r+z)^2$ from the exit:

$$\Delta r_j = \beta \Delta r_{j-1}, \qquad \Delta z_k = \beta' \Delta z_{k-1} \tag{13}$$

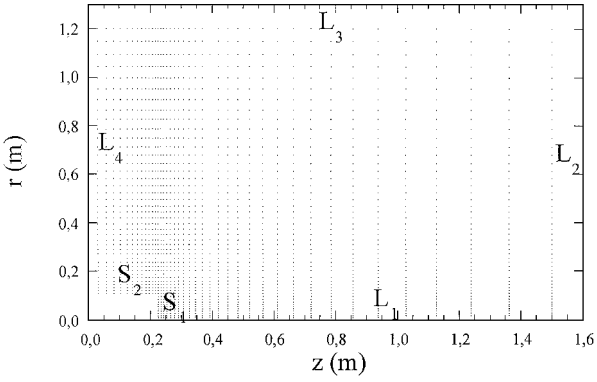

Fig. 7 Scheme of the simulation domain.

The number of grid cells used was 50×40, that is, $\Delta x/\lambda_D$ is in the range [1, 10]. Moreover we have used a weight $w = 6.7 \times 10^8$ because the number of particles per cell was always larger than 100 to minimize the effect of numerical noise. Numerical tests were also performed to ensure that the grid resolution and the number of particles used is sufficient to not affect the steady-state selected values. Computational parameters are reported in Table 3.

The position of the nodes are stored implicitly in a one-dimensional array, rather than in a two-dimensional array. This modification does not affect the computational time significantly, but can save a substantial amount of memory. Figure 7 shows the grid used for the simulations with the necessary boundary conditions. Along S_1 (the thruster exit plane, which also is the inflow boundary) the electric potential is given, equal to ϕ_p, the sum of the accelerator grid's potential and the contribution of the nearby ions (Dirichlet condition). The wall of the thruster (S_2) is assumed to be biased to the spacecraft potential, which is estimated to be $k_B T_e/e$ according to electron and ion currents balance, where T_e is the electron background temperature reported in Table 4. Along L_1 the symmetry boundary condition is given, that is, the radial electric field is set to zero while axial variations in potential are permitted (Neumann condition). Along L_2, L_3, and L_4 the open boundary condition is assumed. This assumption is valid when the domain is sufficiently large:

$$S_1 \rightarrow \phi = \text{const}, \qquad S_2 \rightarrow \phi = \text{const}, \qquad L_1 \rightarrow \frac{\partial \phi}{\partial r} = 0$$

$$L_2, L_4 \rightarrow \frac{\partial^2 \phi}{\partial z^2} = 0, \qquad L_3 \rightarrow \frac{\partial^2 \phi}{\partial r^2} = 0 \tag{14}$$

Particles that reach boundaries other than the symmetry line leave the simulation. Steady state is reached when the number of particles of each species in the simulation domain remains constant while a particle that reaches the symmetry line is replaced by a similar particle with inverted radial velocity.

Injection Condition

At every time step a number of ions Xe^+, Xe^{++} and neutrals are injected into the computational domain using

$$\Delta N_i^+ = \frac{\dot{m}_i^+ \Delta t}{2 m_i w}, \qquad \Delta N_i^{++} = \frac{\dot{m}_i^{++} \Delta t}{2 m_i w}, \qquad \Delta N_n = \frac{\dot{m}_n \Delta t}{2 m_i w} \tag{15}$$

In our code we track the ions, although the neutral flowfield was calculated separately by the DSMC code "SMILE,"[17] and the steady-state result of neutral density, temperature, and velocity are implemented in the present simulation as an overlay technique (Figs. 8 and 9). The radial positions of the ions are calculated on the basis of Eq. (5) by using the standard von Neumann acceptance-rejection method, where the radial coordinates r are sampled uniformly in the interval $[R_1, R_2]$ allowing for the axisymmetry:

$$r = \sqrt{R_1^2 + \left(R_2^2 - R_1^2\right) R_s} \tag{16}$$

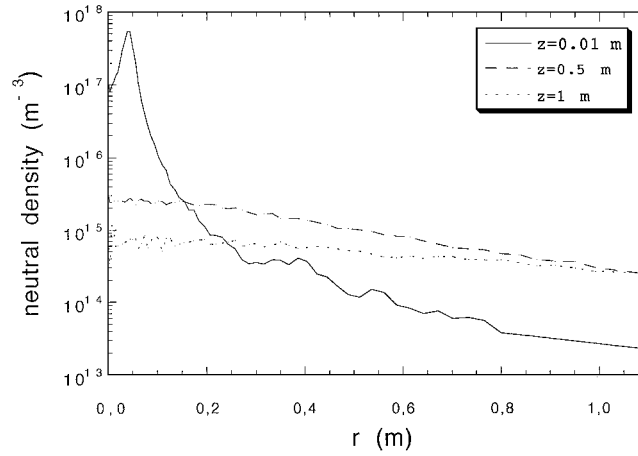

Fig. 8 Neutral number density as a function of radial position for different axial positions.

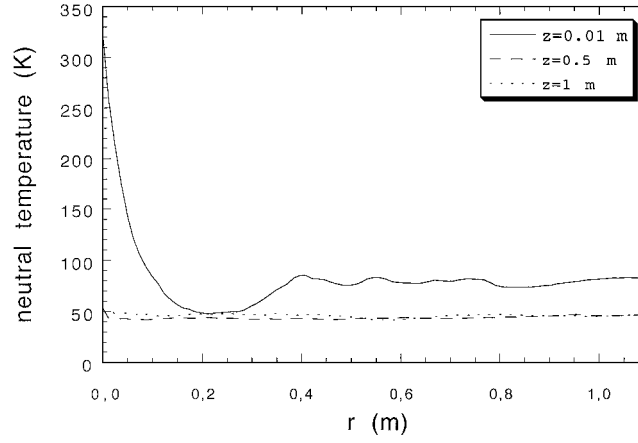

Fig. 9 Neutral temperature as a function of radial position for different axial positions.

Once the radial position is known, we calculate from Eq. (4) the divergence angle in order to estimate the radial and axial drift velocity, whereas on basis of measurements[26] we have assumed a tangential drift velocity of 250 m/s. Furthermore we have added thermal velocity components sampled from Maxwellian distributions based on temperatures $T_r = 8000$ K, $T_z = 34$ eV, and $T_\varphi = 800$ K[5]. The axial temperature is chosen to simulate the presence of a high-energy tail of ions that is seen in laboratory measurements of the ion distribution function,[26] whereas radial and tangential temperature are reasonable estimates based on experimental data.[27] Doubly ionized species are injected with similar thermal component as the singly ionized ions.

Scatter Phase

Within a cell the charge is weighted to the four neighboring grid points, and the volumetric charge density is computed by summing over all macroparticles that are in the cell itself:

$$\rho_{j,k} = \frac{\sum_p Q S_j^{\text{Ruy}}(r_i) S_k^{\text{PIC}}(z_i)}{V_{j,k}}$$

$$\rho_{j+1,k} = \frac{\sum_p Q\left[1 - S_j^{\text{Ruy}}(r_i)\right] S_k^{\text{PIC}}(z_i)}{V_{j+1,k}}$$

$$\rho_{j,k+1} = \frac{\sum_p Q S_j^{\text{Ruy}}(r_i)\left[1 - S_k^{\text{PIC}}(z_i)\right]}{V_{j,k+1}}$$

$$\rho_{j+1,k+1} = \frac{\sum_p Q\left[1 - S_j^{\text{Ruy}}(r_i)\right]\left[1 - S_k^{\text{PIC}}(z_i)\right]}{V_{j+1,k+1}} \tag{17}$$

where we have factorized the weighting function into two parts: the Ruyten charge density conserving shape factor[28] for the radial coordinate that represents a two-dimensional cylindrical system and the PIC shape factor[12] for the axial coordinate that represents a one-dimensional Cartesian system.

Electric Field Evaluation

Once the charge density is computed, the electrostatic potential is determined by solving Poisson's equation:

$$\nabla^2\phi(r,z) + \frac{\rho_i(r,z)}{\varepsilon_0} - \frac{\rho_{\text{ref}}}{\varepsilon_0}\exp\left\{\frac{e[\phi(r,z)-\phi_{\text{tu}}]}{k_B T_e(r,z)}\right\} = 0 \qquad (18)$$

with boundary conditions given by Eq. (14). With the Boltzmann distribution for the electron density, the Poisson equation becomes highly nonlinear. Then the solution is obtained by the iterative Newton–Raphson method[11]:

$$\left(\nabla^2 - \frac{e\rho_{\text{ref}}}{k_B T_e \varepsilon_0}\exp\left\{\frac{e\left[\phi^{(t)}-\phi_{\text{tu}}\right]}{k_B T_e}\right\}\right)\phi^{(t+1)}$$

$$= \left[1 - \frac{e}{k_B T_e}\phi^{(t)}\right]\frac{\rho_{\text{ref}}}{\varepsilon_0}\exp\left\{\frac{e\left[\phi^{(t)}-\phi_{\text{tu}}\right]}{k_B T_e}\right\} - \frac{\rho_i}{\varepsilon_0} \qquad (19)$$

that is discretized allowing for the five-points expression of the Laplacian in cylindrical coordinates. For large and nonuniform meshes grid relaxation techniques are the methods of choice,[11] and in particular we have used a successive-overrelaxation (SOR) scheme with "checkerboard" ordering and Chebyschev acceleration. Given the potential, the electric field $\boldsymbol{E}$ is computed from $\boldsymbol{E} = -\nabla\phi$, which is discretized with the six-points Boris formula[12] for reducing numerical noise and anisotropy. The electric field is interpolated from the nodes to the position of the charged particle using the same weighting scheme of the scatter phase in order to ensure momentum conservation.

Particle Mover

The motion of a charged particle (without collisions) is expressed by

$$\frac{d\boldsymbol{v}_i}{dt} = \left(\frac{Q}{M}\right)_i[\boldsymbol{E} + \boldsymbol{v}_i \times \boldsymbol{B}], \qquad \frac{d\boldsymbol{x}_i}{dt} = \boldsymbol{v}_i \qquad (20)$$

These equations are numerically integrated by the leap-frog scheme. This method is very fast and simple to implement. Moreover the Buneman–Boris leap-frog algorithm[12] is explicit and time centered (enforcing symmetry under time reversal). To minimize the effect of the energy-conservation violation, typical of a PIC-momentum conserving scheme, we have selected the time step according to Hockney's optimum-path condition[11]

$$(\omega_{\text{pi}}\Delta t)_{\text{opt}} = \min\left[\frac{1}{2}\frac{\Delta x}{\lambda_D}, 1\right] \qquad (21)$$

Therefore, $\Delta t = 1.6 \times 10^{-7}$ s and in such a way the Courant–Friedricks–Lewy condition[11] that requires particles to move a small distance relative to the width of local potential gradients in each time step and the stability leap-frog condition[11] are satisfied.

Collision Methodology

The treatment of stage B involves Monte Carlo techniques. In particular, we have implemented the Nanbu test particle Monte Carlo method,[14] which is derived directly from the Boltzmann equation.

Ion-Neutral Collisions

Two kinds of ion-neutral scatterings are considered, the momentum transfer and the charge exchange one:

$$Xe_s + Xe_f^+ \rightarrow Xe_s + Xe_f^+, \qquad Xe_s + Xe_f^+ \rightarrow Xe_s^+ + Xe_f$$

and similarly for double-ionized particles. Our collision technique is an implementation of the test particle Monte Carlo method of Nanbu and Kitatani,[15] where the target distribution function is sampled for a virtual neutral particle and the collision probability is evaluated under the assumption of a polarization potential, introducing a cutoff value of the dimensionless impact parameter:

$$P = n\Delta t(16a/m_i)^{\frac{1}{2}}\pi\beta_\infty^2 \qquad (22)$$

Note that the collision probability is constant in each cell, which makes simulation of the collisions much easier. The second step is to calculate the impact parameter β:

$$\beta = \beta_\infty\sqrt{\boldsymbol{R}_s} \qquad (23)$$

If β is higher than a critical value $\beta_{\text{ex}} = A E^{1/4}$, the scattering process is elastic, and the postcollisional velocities are sampled fulfilling the conservation laws by the following expression:

$$\boldsymbol{v}_i' = \boldsymbol{v}_i - \tfrac{1}{2}[\boldsymbol{g}_{\text{in}}(1-\cos\chi) + \boldsymbol{h}\sin\chi]$$

$$\boldsymbol{v}_n' = \boldsymbol{v}_n + \tfrac{1}{2}[\boldsymbol{g}_{\text{in}}(1-\cos\chi) + \boldsymbol{h}\sin\chi] \qquad (24)$$

where the components of the vector h are given by

$$h_x = \left(g_{\text{in}\,y}^2 - g_{\text{in}\,z}^2\right)^{\frac{1}{2}}\cos\varphi$$

$$h_y = -\frac{g_{\text{in}\,y}g_{\text{in}\,x}\cos\varphi + g_{\text{in}}g_{\text{in}\,z}\sin\varphi}{\left(g_{\text{in}\,y}^2 - g_{\text{in}\,z}^2\right)^{\frac{1}{2}}}$$

$$h_y = -\frac{g_{\text{in}\,z}g_{\text{in}\,x}\cos\varphi - g_{\text{in}}g_{\text{in}\,y}\sin\varphi}{\left(g_{\text{in}\,y}^2 - g_{\text{in}\,z}^2\right)^{\frac{1}{2}}}$$

and the polar angle χ is tabulated as a function of impact parameter (Mitsui, personal communication, 1999). The azimuthal angle φ is sampled uniformly in the interval $[0, 2\pi]$. Otherwise if β is lower than β_{ex} and R_s is lower than the CEX probability (equal to 0.5), the postcollisional velocity (24) is inverted. The values of the two free parameters β_∞ and A are in agreement with Ref. 15 and are reported in Table 4.

Ion-Ion Collisions

Although the mean free path of ion-ion collisions (see Table 4) is greater than the computational dimension, the effect of these coulombic short-range interactions can be important with regard to the mechanism of loss of total energy as suggested by King.[27] To simulate short-range interactions, it is necessary to simulate many collisions that individually cause small angle deflections to occur but collectively cause large changes in particle trajectories. This calculation requires simulating many collisions during each time step and is therefore computationally impractical. For this reason we have implemented these collisions by the theory of Nanbu,[29,30] where a succession of small-angle binary collisions are grouped into a unique binary collision [Eq. (24)] with a large scattering angle given by the following relation:

$$\cos\chi = (1/A)\,\ell n\left(e^{-A} + 2R_s\sinh A\right) \qquad (25)$$

where A is solution of the nonlinear equation

$$\coth A - 1/A = e^{-s} \qquad (26)$$

with s, known as the isotropic parameter, given by

$$s = \frac{\ell n\Lambda}{4\pi}\left(\frac{2Q_i Q_{i'}}{m_i\varepsilon_0}\right)^2 n g_{ii'}^{-3}\Delta t$$

Elastic collisions between ions are not included in the model because collisions between charged particles are dominated by short-range coulomb interactions.

Table 7 SPT-100 plume models characteristics

Model	Rhee–Lewis[1]	Oh et al.[5]	Boyd et al.[7]	Perot et al.[9]	Tajmar et al.[10]	Present model
Domain	2D	3D	2D	2D	3D	2D
Dimension	0.2×0.3 m	$1 \times 1 \times 2.6$ m	1×1.3 m	0.5×1 m	$2 \times 2 \times 2$ m	1.2×1.5 m
Macroions	10^5	10^6	8×10^5	10^5	10^6	10^6
Species simulated	Xe^+	Xe, Xe^+, e^-	Xe, Xe^+, Xe^{++}, e^-	Xe, Xe^+, Xe^{++}, e^-	Xe, Xe^+, Xe^{++}, e^-	Xe, Xe^+, Xe^{++}, e^-
Field solver	Poisson equation	Quasi-neutrality hypothesis	Quasi-neutrality hypothesis	Poisson equation	Quasi-neutrality hypothesis	Poisson equation
Electrons model	Isothermal, unmagnetized collisionless	Isothermal, unmagnetized collisionless	Not isothermal, magnetized collisionless	Isothermal, unmagnetized collisionless	Isothermal, unmagnetized collisionless	Not isothermal, unmagnetized collisionless
Ion-neutral collision model	Point source approximation	DSMC	DSMC	TPMC	DSMC	TPMC
Ion coulombic interactions	No	No	No	No	No	Yes
Surface-sputtering model	No	Yes	No	No	No	No

Neutral-Neutral Collisions

These collisions are processed in the "SMILE" code[17] by the variable hard sphere (VHS) model that employs the scattering law of hard sphere. Diameters of the colliding particles are inversely proportional to the relative translational energy of the pair:

$$\sigma_T \equiv \pi d^2 \approx \left(m_n g^2 / 4\right)^{-\gamma}, \qquad b = d\cos(\chi/2) \tag{27}$$

where σ_T is the total cross section, $d = 5.74 \times 10^{-10}$ m is the molecular diameter, b is the impact parameter, χ is the deflection angle, $\gamma = 0.62$ is a factor determining the potential stiffness known as viscosity temperature exponent. The characteristics of the present along model with those of the preceding simulations of the SPT-100 plume are summarized in Table 7.

Results and Discussion

In this section we present the simulation results obtained assuming laboratory ambient plasma (see Table 6) that are compared, where possible, with experimental measurements. The off-axis and backflow regions are areas where measurements are most difficult because of low signal and chamber interference effect.

Computationally, the steady state is reached after about 40,000 time steps when the CEX ions have crossed the simulation domain, but we have noted that after 2000 time steps the local values of macroscopic quantities do not change anymore.

At this moment the total number of macroions simulated is about 10^6. Further numerical tests confirmed that the results were insensitive to the number of particles in the simulation and to the number of the iterations once the plume had reached a steady state. The execution time (code written in FORTRAN 90) is about four days on UNIX alpha workstation with a processor of 400 Mhz. In Figs. 10a and 10b a snapshot is reported of the position of a limited number of marker ions at two different times during the simulation.

Note that ions exit the thruster channel as a narrow beam with a divergence angle of about 40 deg to the thruster axis and as a CEX component out of the primary beam and propagating both up- and downstream.

In Figs. 11a and 11b the common logarithm of ion charge density at the same times is reported. As can be seen, the ions propagate under the effect of self-consistent electric field, magnetic applied field, and collisions with neutrals and ions until a stationary state is reached when the outflow balances the ion emission. A significant component of backflow appears, as well as significant expansion in the radial direction. The effect of charge-exchange collisions is clearly detectable in Fig. 12, which plots the $v_r - v_z$ phase space at steady state. CEX ions are visible as a wing of low-velocity ions. Although CEX ions begin with relatively low speed, the plume's potential structure tends to drive these ions sideways and backward, toward the spacecraft rather than away from it. These CEX ions can then impact spacecraft surfaces, causing contamination and erosion damage. This is confirmed by the Figs. 13a and 13b, where we have reported the two components of ionic velocity as a function of radial position for different values of axial position. By inspecting the plot

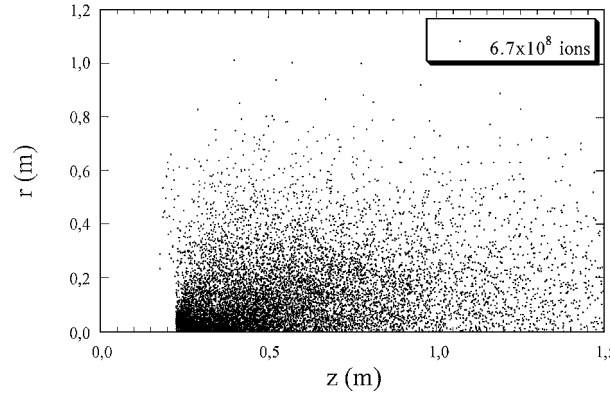

Fig. 10a Configuration space plot of marker ions at $t = 3.2 \times 10^{-5}$ s.

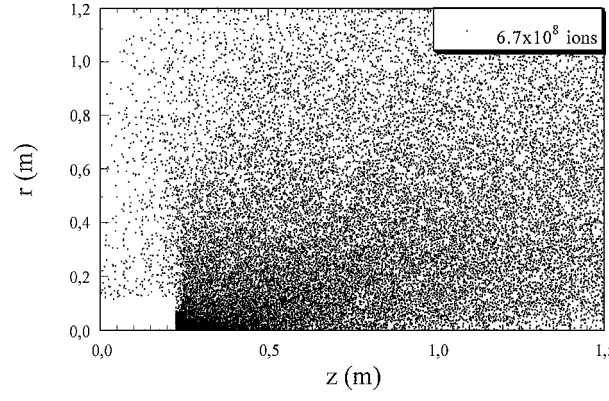

Fig. 10b Configuration space plot of marker ions at $t = 1.6 \times 10^{-4}$ s.

of the axial velocity, one can notice that particles in the backflow region have a moderate velocity directed toward the payload. Also, we can see that the position dependence of axial velocity is coherent with a free molecular expanding beam. The plot of radial velocity shows a strong increment in the very near region in accord with measurements of Manzella.[26]

Figure 14 illustrates the electric potential at the steady state. We can note a fall of 50 V between the exit plane and the stagnation region, where a potential well develops spontaneously. The lobe structures seen directly on the side of the thruster exit are produced by the charge-exchange plasma. The plasma potential is compared with measurements[8] at an axial distance of 48 cm in Fig. 15. The agreement is qualitatively good. Figures 16a and 16b are plots of electric field components. We note the negative axial field and a strong radial field in the backflow region causing the "dangerous" drift of CEX ions to the surfaces.

To discuss the influence of coulomb collisions, we have reported in Fig. 17 the plasma potential as a function of axial distance from

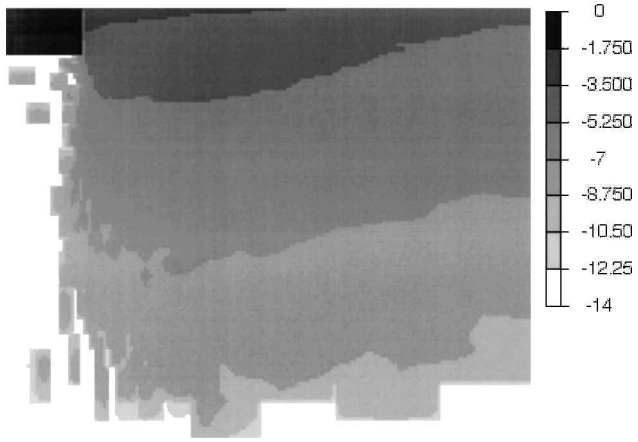

Fig. 11a Common logarithm of ionic charge density at $t = 3.2 \times 10^{-5}$ s.

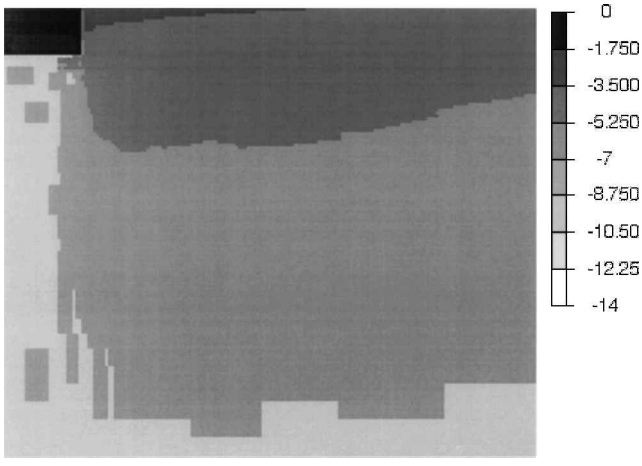

Fig. 11b Common logarithm of ionic charge density at $t = 1.6 \times 10^{-4}$ s.

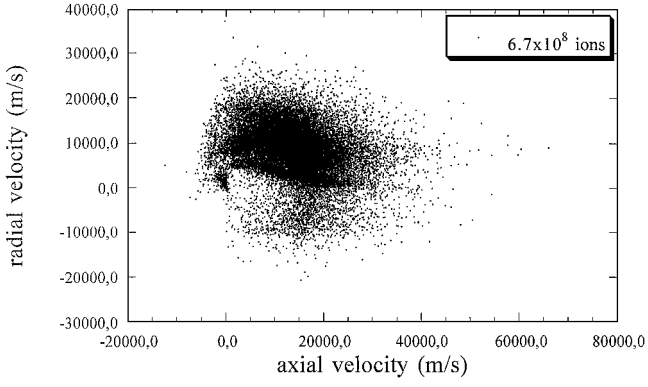

Fig. 12 Phase space plot of marker ions at $t = 1.6 \times 10^{-4}$ s.

the thruster at a radial distance of 3.5 cm from the thruster centerline. We can see that the curves with and without coulomb collisions are substantially identicals. It will be expected that coulomb collisions will be important in the very near-field plume region where the electron temperature is quite high.

In Fig. 4 the Xe^{+} density is reported as a function of angle at a radial distance of 0.5 m from the thruster. In general we can anticipate that the behavior of singly and doubly ionized particles is qualitatively close. The simulation results agree fairly well with experimental data.[31]

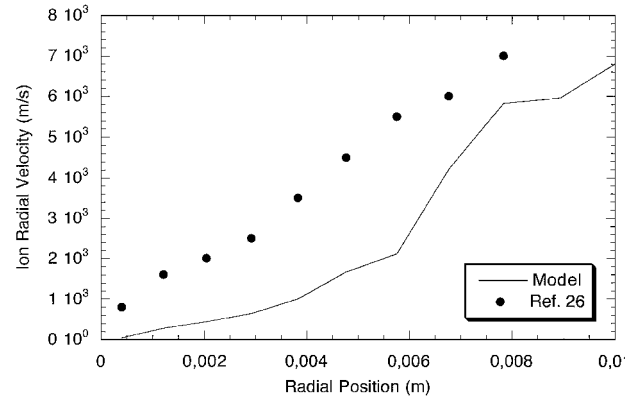

Fig. 13a Radial ion velocity as a function of radial position for different axial positions.

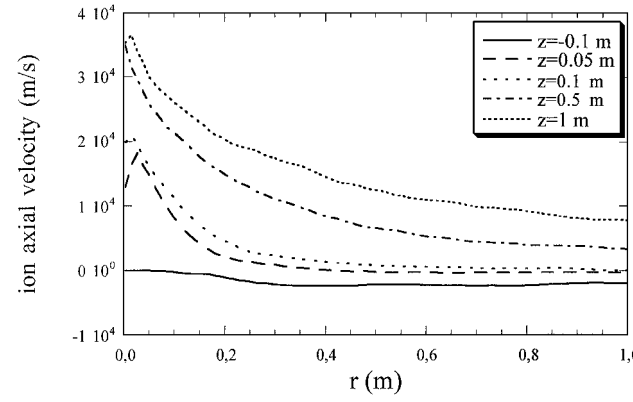

Fig. 13b Axial ion velocity as a function of radial position for different axial positions.

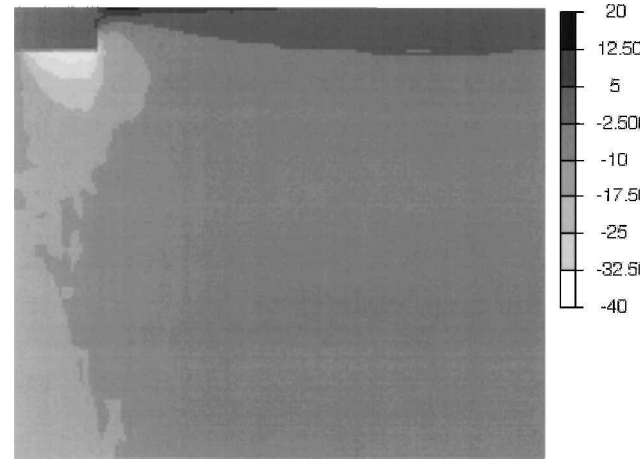

Fig. 14 Equipotential lines at the steady state.

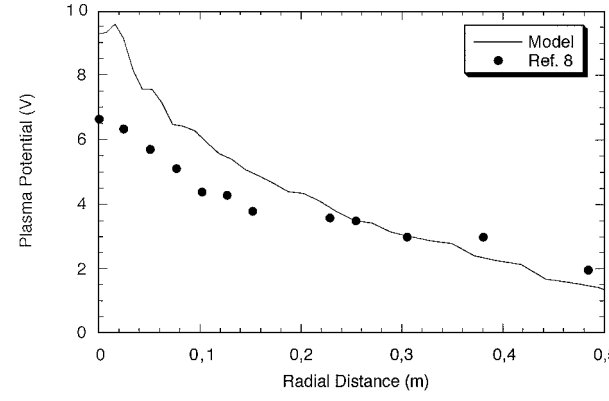

Fig. 15 Comparison of potential at an axial distance of 48 cm.

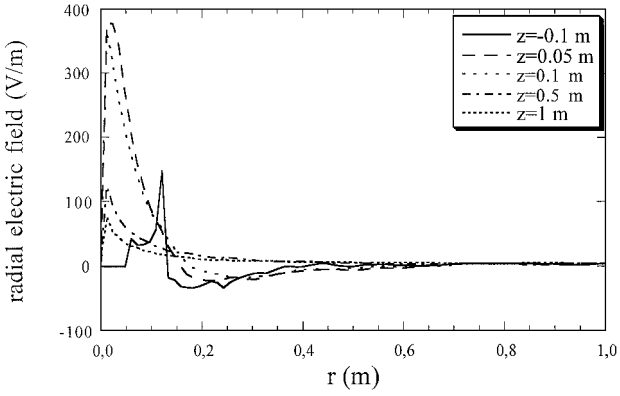

Fig. 16a Radial electric field as a function of radial position for different axial positions.

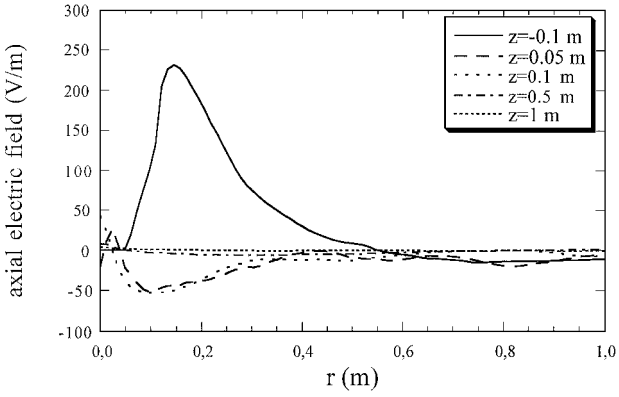

Fig. 16b Axial electric field as a function of radial position for different axial positions.

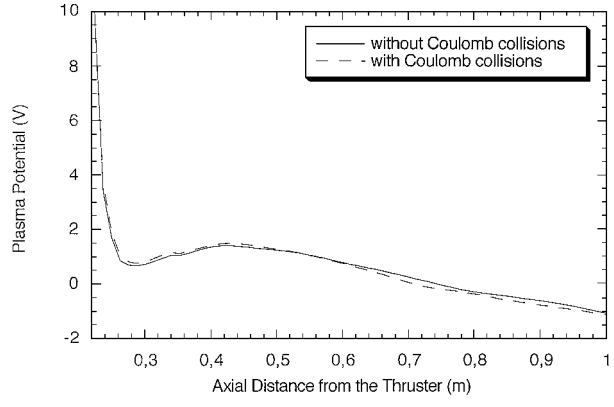

Fig. 17 Comparison of potential with and without coulomb collisions at a radial distance of 3.5 cm.

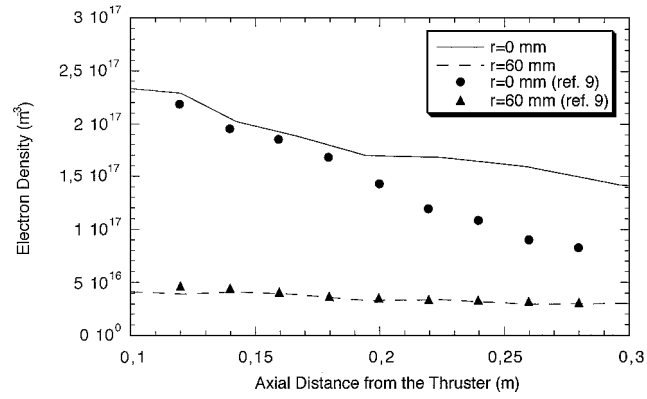

Fig. 18 Comparisons of axial profiles of electron density at different radial locations.

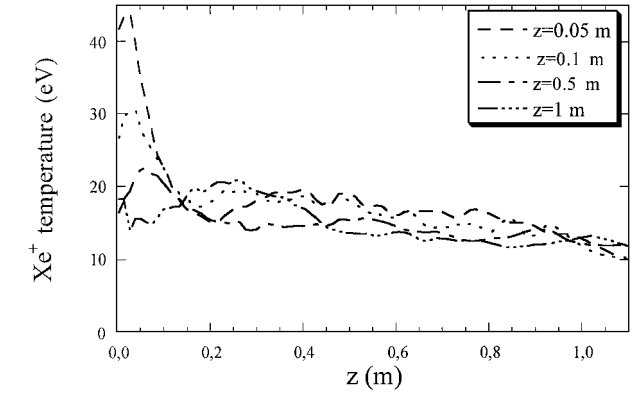

Fig. 19 Xe^+ temperature as a function of radial position for different axial positions.

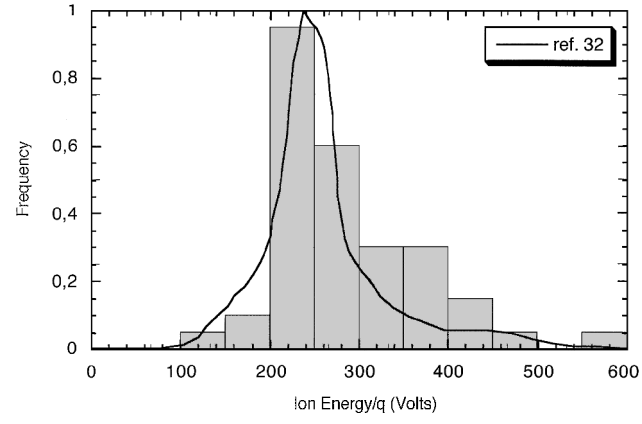

Fig. 20 Energy distribution of ions at $z = 0.5$ m from the thuster exit plane.

In Fig. 5 the Xe^+ temperature is reported to start increasing very quickly with z for short distances from the outlet shape, reaching values of about 30–50 eV and decreasing slowly for higher z. Higher temperatures are observed for doubly ionized particles. These values have to be interpreted with care. In particle methods the temperature is essentially computed as the variance of the velocity distribution function, which is measured from the total internal energy. In a plasma with a significant degree of charge exchange, the velocity distribution functions are very wide. This is the cause of the high ion temperature in the near plume region, where the CEX ions are numerous.

Figures 18 and 19 show comparisons of electron number density and electron temperature with experiments in the very near region of the plume. These figures show good agreement with Perot's[9] and Kim's[24,25] measurements, respectively. The electron temperature, reported in Fig. 19, follows, on the basis of the adiabatic equation, the electron density and is indeed strongly dependent on position. The usual assumption of a quasi-uniform electron gas with temperature about 3–4 eV holds only quite far from the thruster.

The present plasma model was used to calculate the energy distribution of ions at $z = 0.5$ m from the thruster exit plane. Results are compared with experimental data[32] in Fig. 20.

Conclusions

A hybrid two-dimensional, 3V axisymmetric PIC/TPMC numerical code has been developped for the simulation of plasma plume expansions in various conditions and in ambient plasmas. The model takes into account the effects of nonisothermal electron temperature and the effects of violations of the quasi-neutral plasma hypothesis in the very near-field plume region. Moreover the ion coulombic interactions are included in the code to take in account the mechanism of loss of total energy. Comparison of model results with existing experimental data suggests that the simulation is consistent with the physics of the very near-field plume region.

Acknowledgments

This work was partially supported by the ESA through ESA/ESTEC Contract 12736/97/NL/PA. The authors thank Leonardo Biagioni at CentroSpazio for providing data of injection conditions used in this paper and for data and help with the thruster geometry and Gennady Markelov at Institute of Theoretical and Apllied Mechanics for data of the neutral particles.

References

[1]Rhee, M. S., and Lewis, M. J., "Numerical Simulation of Stationary Plasma Thruster Exhaust Plume," AIAA Paper 95-2928, July 1995.

[2]Oh, D. Y., and Hastings, D. E., "Axisymmetric PIC-DSMC Simulation of SPT Plume," IEPC Paper 95-160, Sept. 1995.

[3]Oh, D. Y., and Hastings, D. E., "Experimental Verification of a PIC-DSMC Model for Hall Thruster Plumes," AIAA Paper 96-3196, July 1996.

[4]Oh, D. Y., and Hastings, D. E., "Three Dimensional PIC-DSMC Simulation of Hall Thruster Plume and Analysis for Realistic Spacecraft Configurations," AIAA Paper 96-3299, July 1996.

[5]Oh, D. Y., Hastings, D. E., Marrese, C. M., Haas, J. M., and Gallimore, A. D., "Modeling of Stationary Plasma Thruster-100 Thruster Plume and Implications for Satellite Design," *Journal of Propulsion and Power*, Vol. 15, No. 2, 1999, pp. 345–357.

[6]Boyd, I. D., and VanGilder, D. B., "Particle Simulation of the SPT-100 Hall Thruster Plume," AIAA Paper 98-3797, 1998.

[7]Boyd, I. D., VanGilder, D. B., and Keidar, M., "Modeling Hall Thruster Plumes Using Particle Methods," AIAA Paper 99-2294, June 1999.

[8]Boyd, I. D., VanGilder, D. B., and Keidar, M., "Particle Simulation of a Hall Thruster Plume," *Journal of Spacecraft and Rockets*, Vol. 37, No. 1, 2000, pp. 129–136.

[9]Perot, C., Gascon, N., Bechu, S., Lasgorceix, P., Dudeck, M., Garrigues, L., and Boeuf, J. P., "Characterization of a Laboratory Hall Thruster with Electrical Probes and Comparison with a 2D Hybrid PIC-MCC Model," AIAA Paper 99-2716, June 1999.

[10]Tajmar, M., Gonzàlez, J., and Hilgers, A., "Modelling of Spacecraft Environment Interactions on SMART-1," AIAA Paper 2000-3526, July 2000.

[11]Eastwood, J. W., and Hockney, R. W., *Computer Simulation Using Particles*, McGraw–Hill, New York, 1981, pp. 171, 179, and 321.

[12]Birdsall, C. K., and Langdon, A. B., *Plasma Physics via Computer Simulation*, McGraw–Hill, New York, 1985, pp. 21, 38, and 328.

[13]Birdsall, C. K., "Particle-in-Cell Charged Particle Simulation, Plus Monte Carlo Collisions with Neutral Atoms, PIC-MCC," *IEEE Transactions on Plasma Science*, Vol. 19, No. 2, 1991, pp. 65–85.

[14]Nanbu, K., "Direct Simulation Scheme Derived from the Boltzmann Equation. I. Monocomponent Gases," *Journal of the Physical Society of Japan*, Vol. 49, No. 5, 1980, pp. 2042–2049.

[15]Nanbu, K., and Kitatani, Y., "An Ion-Neutral Species Collision model for Particle Simulation of Glow Discharge," *Journal of Physics D: Applied Physics*, Vol. 28, No. 2, 1995, pp. 324–330.

[16]Bird, G. A., *Molecular Gas Dynamics and the Direct Simulation of Gas Flows*, Clarendon, Oxford, 1994, p. 203.

[17]Ivanov, M. S., Markelov, G. N., and Gimelshein, S. F., "Statistical Simulation of Reactive Rarefied Flows: Numerical Approach and Applications," AIAA Paper 98-2669, June 1998.

[18]Boccaletto, L., "Electric Thruster Technologies SPT-100 Ion Inflow Data," CentroSpazio, Rept. WP-3, ESA/ESTEC 12736/97/NL/PA, Pisa, Italy, Dec. 1999.

[19]Bishaev, A. M., and Kim, V. P., "Local Plasma Properties in a Hall-Current Accelerator with an Extended Acceleration Zone," *Soviet Physics—Technical Physics*, Vol. 23, No. 9, 1978, pp. 1055–1057.

[20]Garrigues, L., Boyd, I. D., and Boeuf, J. P., "Computation of Hall Thruster Performance," IEPC Paper 99-098, Oct. 1999.

[21]Morozov, A. I., Bugrova, A. I., and Ermolenko, V. A., "A Study of Ion Formation in a Hall Accelerator," *Soviet Physics—Technical Physics*, Vol. 33, No. 2, 1988, pp. 185–187.

[22]Cedolin, R. J., Hargus, W. A., Jr., Hanson, R. K., and Capelli, M. A., "Laser-Induced Fluorescence Diagnostics for Xenon Hall Thrusters," AIAA Paper 96-2986, July 1996.

[23]Gulczinski, F. S., III, "Examination of the Structure and Evolution of Ion Energy Properties of a 5 kW Class Laboratory Hall Effect Thruster at Various Operational Conditions," Ph.D. Dissertation, Dept. of Aerospace Engineering, Univ. of Michigan, Ann Arbor, MI, Aug. 1999.

[24]Kim, S., Foster, J. E., and Gallimore, A. D., "Very-Near-Field Plume Study of a 1.35 kW SPT-100," AIAA Paper 96-2972, July 1996.

[25]Kim, S. W., "Experimental Investigation of Plasma Parameters and Species-Dependent Ion Energy Distribution in the Plasma Exhaust Plume of a Hall Thruster," Ph.D. Dissertation, Dept. of Aerospace Engineering, Univ. of Michigan, Ann Arbor, MI, Aug. 1999.

[26]Manzella, D. H., "Stationary Plasma Thruster Ion Velocity Distribution," AIAA Paper 94-3141, 1994.

[27]King, L. B., "Transport-Property and Mass Spectral Measurements in the Plasma Exhaust Plume of a Hall-Effect Space Propulsion System," Ph.D. Dissertation, Dept. of Aerospace Engineering, Univ. of Michigan, Ann Arbor, MI, May 1998.

[28]Ruyten, W. M., "Density-Conserving Shape Factors for Particle Simulations in Cylindrical and Spherical Coordinates," *Journal of Computational Physics*, Vol. 105, 1993, pp. 224–232.

[29]Nanbu, K., "Theory of Cumulative Small-Angle Collisions in Plasmas," *Physics Review E*, Vol. 55, No. 4, 1997, pp. 4642–4652.

[30]Nanbu, K., and Yonemura, S., "Weighted Particles in Coulomb Collision Simulations Based on the Theory of a Cumulative Scattering Angle," *Journal of Computational Physics*, Vol. 145, No. 2, 1998, pp. 639–650.

[31]King, L. B., and Gallimore, A. D., "Ionic and Neutral Particle Transport Property Measurements in the Plume of an SPT-100," AIAA Paper 96-2712, July 1996.

[32]Boyd, I. D., "A Review of Hall Thruster Plume Modeling," AIAA Paper 2000-0466, Jan. 2000.

I. D. Boyd
Associate Editor